Remote Sensing of Environment 221 (2019) 773–783

Contents lists available at ScienceDirect

Remote Sensing of Environment

journal homepage: www.elsevier.com/locate/rse

Achieving high-resolution thermal imagery in low-contrast lake surface waters by aerial remote sensing and image registration

Abolfazl Irani Rahaghi[a,*], Ulrich Lemmin[a], Daniel Sage[b], David Andrew Barry[a]

[a] Ecological Engineering Laboratory (ECOL), Environmental Engineering Institute (IIE), Faculty of Architecture, Civil and Environmental Engineering (ENAC), Ecole Polytechnique Fédérale de Lausanne (EPFL), 1015 Lausanne, Switzerland

[b] Biomedical Imaging Group (BIG), School of Engineering (STI), Ecole Polytechnique Fédérale de Lausanne (EPFL), 1015 Lausanne, Switzerland

ARTICLE INFO

Keywords:
Aerial remote sensing
Thermal imagery
Lake surface water temperature
Image registration
Uncooled infrared camera
Lake Geneva

ABSTRACT

A two-platform measurement system for realizing airborne thermography of the Lake Surface Water Temperature (LSWT) with ~0.8 m pixel resolution (sub-pixel satellite scale) is presented. It consists of a tethered Balloon Launched Imaging and Monitoring Platform (BLIMP) that records LSWT images and an autonomously operating catamaran (called ZiviCat) that measures in situ surface/near surface temperatures within the image area, thus permitting simultaneous ground-truthing of the BLIMP data. The BLIMP was equipped with an uncooled InfraRed (IR) camera. The ZiviCat was designed to measure along predefined trajectories on a lake. Since LSWT spatial variability in each image is expected to be low, a poor estimation of the common spatial and temporal noise of the IR camera (nonuniformity and shutter-based drift, respectively) leads to errors in the thermal maps obtained. Nonuniformity was corrected by applying a pixelwise two-point linear correction method based on laboratory experiments. A Probability Density Function (PDF) matching in regions of overlap between sequential images was used for the drift correction. A feature matching-based algorithm, combining blob and region detectors, was implemented to create composite thermal images, and a mean value of the overlapped images at each location was considered as a representative value of that pixel in the final map. The results indicate that a high overlapping field of view (~95%) is essential for image fusion and noise reduction over such low-contrast scenes. The in situ temperatures measured by the ZiviCat were then used for the radiometric calibration. This resulted in the generation of LSWT maps at sub-pixel satellite scale resolution that revealed spatial LSWT variability, organized in narrow streaks hundreds of meters long and coherent patches of different size, with unprecedented detail.

1. Introduction

Lake Surface Water Temperature (LSWT) is a powerful indicator of meteorological and climatological forcing dynamics of inland water bodies (Livingstone and Dokulil, 2001; Adrian et al., 2009). Resolving the spatiotemporal variability of LSWT, particularly on smaller scales, is essential in order to advance the understanding and quantification of a wide range of processes in lakes, such as ecosystem dynamics (Beaulieu et al., 2013; Bonvin et al., 2013; Bauersachs et al., 2015; Binding et al., 2018), climate change (e.g., Lemmin and Amouroux, 2013; O'Reilly et al., 2015; Woolway and Merchant, 2018), and numerical weather prediction (Balsamo et al., 2012; Le Moigne et al., 2016). Since LSWT and air-water heat exchange are strongly coupled (Woolway et al., 2015; Tozuka et al., 2017), spatial heterogeneity of LSWT affects area-averaged surface heat flux estimates (Mahrt and Khelif, 2010; Rahaghi et al., 2018a). Data sources for LSWT mapping include remote sensing and in situ measurements. Depending on cloud cover, satellite data can depict large-scale thermal patterns, but not sub-pixel processes. Hereinafter, sub-pixel scale refers to horizontal structures ranging from O (1 m) to O(100 m). Satellite thermal images are usually validated against point measurements (e.g., Oesch et al., 2005; Riffler et al., 2015; Dörnhöfer and Oppelt, 2016; Torbick et al., 2016; Ptak et al., 2017), which are considered to be representative for a sizeable surface area (typical pixel size ~1 km^2). Airborne thermography using an infrared camera (IR) can spatially better resolve sub-pixel scale LSWT patterns.

In recent years, commercial and scientific applications of IR cameras have grown substantially (e.g., Mounier, 2011; Lahiri et al., 2012). Thermal detectors used in IR cameras can be cooled or uncooled (Williams, 2009; Vollmer and Möllmann, 2011). Cooled cameras provide a higher and more stable thermal sensitivity compared to uncooled

* Corresponding author.
E-mail addresses: abolfazl.iranirahaghi@epfl.ch (A. I. Rahaghi), ulrich.lemmin@epfl.ch (U. Lemmin), daniel.sage@epfl.ch (D. Sage), andrew.barry@epfl.ch (D.A. Barry).

https://doi.org/10.1016/j.rse.2018.12.018
Received 9 March 2018; Received in revised form 19 November 2018; Accepted 11 December 2018

detectors, but they are more expensive and heavier than uncooled ones; this limits their use on small airborne platforms. Uncooled cameras are an adequate choice for many airborne environmental applications (e.g., Torgersen et al., 2001; Handcock et al., 2006; Haselwimmer et al., 2013; Hernandez et al., 2014; Tamborski et al., 2015; Neale et al., 2016) due to their lower price, compactness, portability, and high spatial and good temperature resolutions (Kruse, 1997; Vollmer and Möllmann, 2011). However, LSWT thermography must take into consideration the following: When moving platforms, such as aircrafts, are used to cover a broader area (e.g., Ferri et al., 2000; Tonolla et al., 2012; Haselwimmer et al., 2013; Emery et al., 2014; Castro et al., 2017), registration (stitching) of the image sequence is frequently required. Atmospheric boundary layer conditions under which thermal imagery is carried out, are constantly changing, due to spatio-temporal variation in air temperature, humidity and atmospheric aerosol concentration. This, together with a typical thermography altitude of O (100 m) to O(1 km), makes it more challenging to obtain a reliable estimation of the atmospheric transmission coefficient than under controlled laboratory conditions. Therefore, in situ ground-truthing is needed for the radiometric calibration of airborne thermography. The spatial variation of temperature, and consequently the grey value contrast in an IR image, is expected to be low over natural waters. To properly address the effects of these particular conditions requires advanced image processing.

The core of an uncooled IR sensor (microbolometer) consists of a two-dimensional detector matrix, called the Focal Plane Array (FPA). Optical, electronic and mechanical components of the camera may affect the irradiance outputs (Milton et al., 1985; Vollmer and Möllmann, 2011; Budzier and Gerlach, 2015). Error sources include spatial noise, called nonuniformity, and temporal noise, called shutter-based drift (offset) (Nugent et al., 2013; Budzier and Gerlach, 2015). Nonuniformity in thermal imagery results from the different photo responses of individual detectors in the FPA for the same incident radiation. Thermal cameras usually try to correct this internally by periodically placing a mechanical shutter with a uniform temperature between the camera and the lens (FLIR, last accessed 25 October 2018). This Flat Field Correction (FFC) enhances the internal offset coefficients of the camera, subsequently providing a more uniform image. During the implementation procedure, which takes ~2 s, the thermal imagery is frozen. However, the missing internal correction between the sequential FFC operations results in a thermal drift in the images. Nonuniformity and drift corrections must be performed prior to camera temperature calibration (Vollmer and Möllmann, 2011). Quantification of these noise sources, and consequently correcting the camera output, requires details of internal signal processing of the microbolometer array, and other parameters, e.g., camera internal temperature and sensor temperature information that is usually not available. Therefore, a calibration model is needed for the camera.

Calibration models require an adjustable constant scene temperature (e.g., Perry and Dereniak, 1993; Marinetti et al., 1997), rely on the IR camera internal information (e.g., Parra et al., 2011; Nugent et al., 2013; Nugent and Shaw, 2014; Budzier and Gerlach, 2015), or use scene-based algorithms (e.g., Torres et al., 2005, 2006; Mesas-Carrascosa et al., 2018), These algorithms are best suited for thermal imagery of high temperature contrast fields. However, satellite images of lake surface waters show that LSWT differences are generally very small, typically much less than 5 °C. Therefore, this kind of calibration cannot be used for image fusion and registration of over-lake IR images.

Previous studies in Lake Geneva (our study site) used Advanced Very High Resolution Radiometer (AVHRR) satellite data to investigate the diurnal/nocturnal LSWT evolution of this lake (Oesch et al., 2005, 2008). Due to the limited spatial resolution, it was suggested that the observed warm/cold LSWT regions could possibly be due to the development or attenuation of a diurnal thermocline, lake breezes and/or large-scale summertime circulation patterns resulting from temporally and spatially variable wind forcing patterns over the lake (Lemmin and D'Adamo, 1996). Therefore, resolving sub-pixel scale LSWT patterns can help reduce the uncertainties in the LSWT data interpretation of satellite-based investigations.

The objective of the present study is to demonstrate the feasibility of using a two-platform measurement system that we developed, together with proposed image processing algorithms, to obtain LSWT patterns at sub-pixel satellite scales on Lake Geneva. The two-platform measurement system consists of a Balloon Launched Imaging and Monitoring platform (BLIMP) and an autonomously operating catamaran called ZiviCat. We implemented an image processing workflow including NonUniformity Correction (NUC), drift correction, and denoising through image fusion. A feature matching-based algorithm was used for image registration (stitching). The proposed methodology was validated by comparing the corrected grey values and the simultaneous in situ high-resolution water temperature data that were obtained by the ZiviCat.

2. Materials and methods

2.1. Study site

Located between Switzerland and France, Lake Geneva (Local name: *Lac Léman*) is a large, deep perialpine lake at a mean surface altitude of 372 m. It is approximately 70 km long, with a maximum width of 14 km, a surface area of 582 km^2 and a volume of 89 km^3 (Fig. 1). To avoid the effect of coastal mixing on the temporal and spatial patterns of LSWT, we present results for an area sufficiently far from the shores. Therefore, land features, which typically have high contrast in both visible and IR bands and can be helpful for image stitching and fusion (e.g., Tamborski et al., 2015), are, unfortunately, absent in the areas of interest of this study (see inset in Fig. 1).

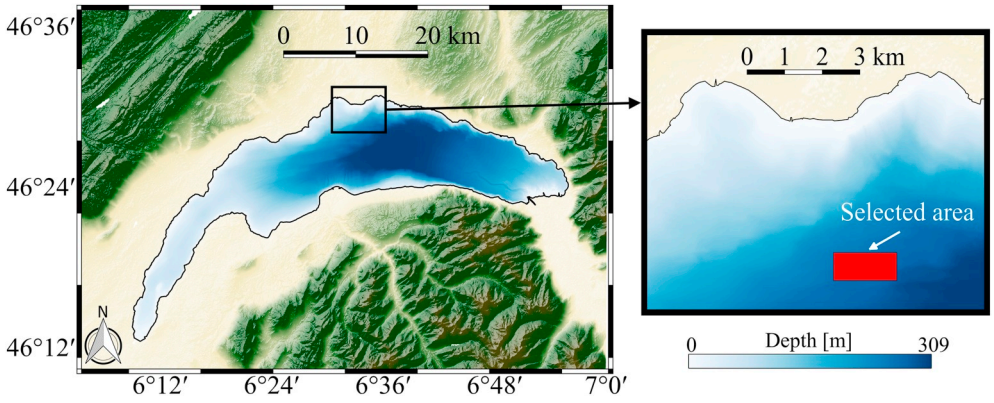

Fig. 1. Location and bathymetry (see the legend at the bottom of the zoom inset) of Lake Geneva, adapted from a public domain satellite image (NASA World Wind, last accessed 25 October 2018) and from bathymetry data (SwissTopo, last accessed 25 October 2018). The red rectangle in the inset indicates the area of the present study. (For interpretation of the references to color in this figure legend, the reader is referred to the web version of this article.)

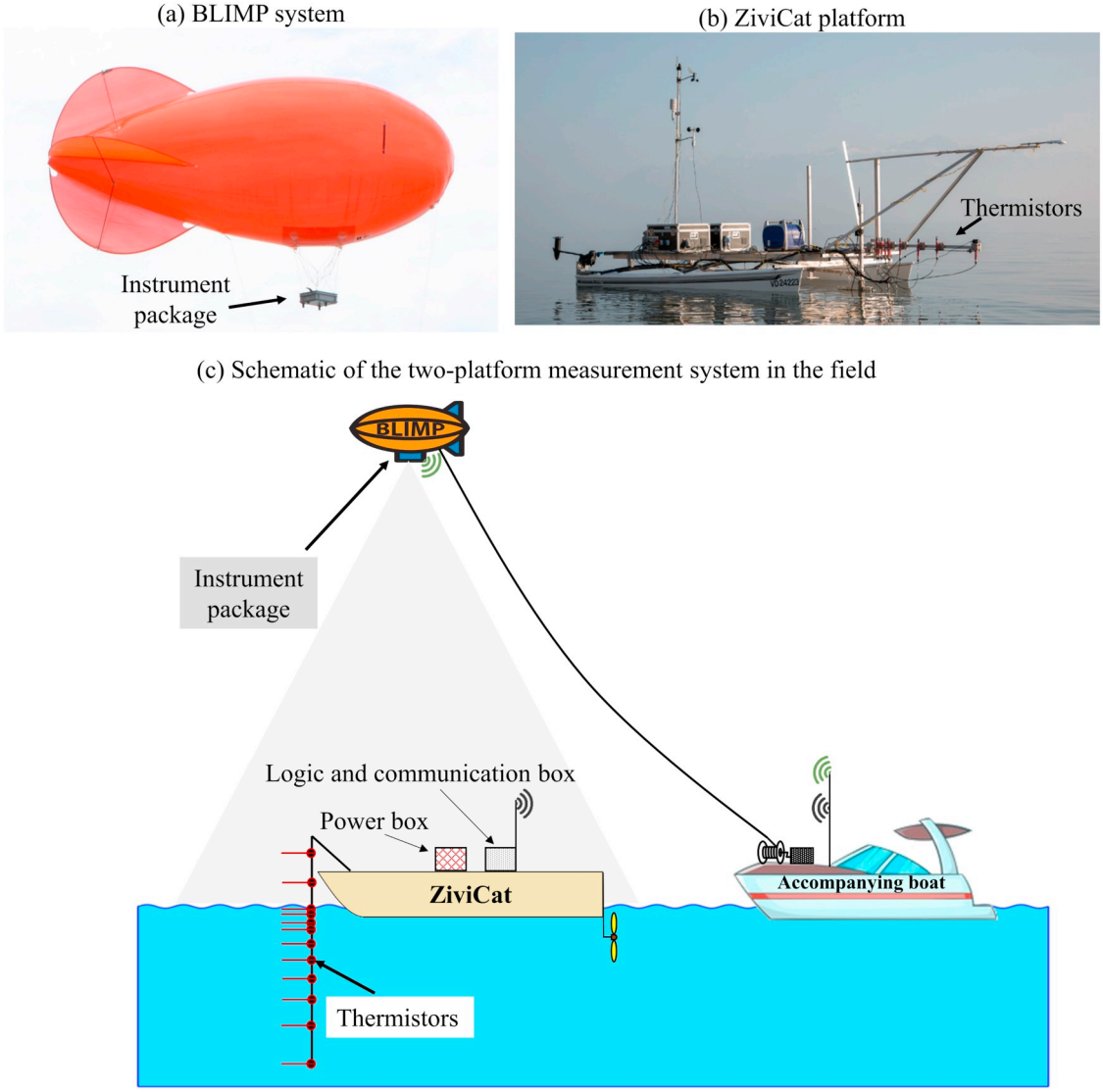

Fig. 2. The two-platform measurement system used in this field study: (a) BLIMP for airborne imagery, (b) ZiviCat catamaran for in situ measurements, and (c) schematic of the combined measurement system. A small balloon (volume 9 m^3) that carries the BLIMP instrument package beneath it, is tethered to a winch on a boat accompanying the ZiviCat. The thermistor spar of the ZiviCat, which is tilted horizontally in (b) for navigation in shallow areas, is rotated vertically for measurements and includes 10 thermistors to measure the near-surface layer (down to 1.5 m depth) temperature profiles, as shown in (c).

2.2. Measurement platforms and field measurement procedures

Field measurement campaigns were carried out in Lake Geneva (Fig. 1) using our two-measurement platform system consisting of: (i) an airborne package for thermal imagery called BLIMP (Fig. 2a), and (ii) an autonomously operating catamaran called ZiviCat (Fig. 2b) for in situ measurements.

A small balloon, carrying the BLIMP instrument package suspended beneath it (grey box in Fig. 2a), was tethered to a winch on the boat accompanying the ZiviCat (Fig. 2c). The balloon's height could be controlled (typically between 300 m and 800 m). Varying the height allows for optimizing between high spatial resolution and the size of the covered area. The BLIMP package included a *FLIR Tau2 LWIR* camera (640 × 512 pixel resolution, 14-bit digital output) and a *Raspberry Pi* RGB camera (used for visual inspection and verification; Liardon and Barry, 2017), as well as other equipment for its position (GPS), orientation, tilt angles (Inertial Measurement Unit; IMU), height, and communication with the boat. The system used either *User Datagram Protocol (UDP)* communication through a mobile network via a *4G* module, or serial radio transmission using an *XBee Pro* 100 mW module for real-time monitoring of the BLIMP imagery on the boat. All data were recorded internally in the BLIMP package. Compared to other aerial systems such as aircrafts or drones, the BLIMP system is less affected by vibration and tilting, as we confirmed by testing with our custom-made autonomous drone (Liardon et al., 2017). To minimize camera movement, a self-balancing attachment system was used (Picavet rigging, last accessed 25 October 2018) that allows for a passive stabilization even under moderate wind speeds. However, in our study, measurements were made under weak wind conditions, when LSWT spatial patterns are more likely to occur and when data are less contaminated by surface waves and BLIMP lateral movements.

Simultaneous ground-truthing of the BLIMP data was achieved using the ZiviCat, an autonomously operating catamaran. It can measure in situ near-surface water temperatures (main parameter in this study), as well as lake current profiles, radiative heat flux, and surface momentum flux for physical limnology investigations. In the near-surface water layer, ten RBRsolo temperature sensors (RBR, last accessed 25 October 2018) with an accuracy of 0.002 °C were mounted on a 2-m long spar and measured water temperature profiles with a frequency of up to 1 Hz in the near-surface layer (1.5 m). Thermistors were more

closely spaced near the surface (shown with the arrow in Fig. 2b and c). The thermistor spar was mounted well forward of the catamaran to avoid hull disturbances. The ZiviCat also carried equipment for position (GPS), stability (IMU), data recording, and communication (Logic and communication box in Fig. 2c). This allowed for real-time data control, correction, and analysis on the boat that accompanied the ZiviCat. Details of the systems and sensors are presented in (Barry et al., 2018).

Field campaigns were conducted during the daytime and over predefined areas of Lake Geneva to test the feasibility of the combined BLIMP-ZiviCat system. To assess the performance of the measurement platforms and the proposed image processing procedure, the results of the 18 March 2016 campaign are presented here as an example. Similar LSWT patterns were observed during the other campaigns in other parts of the lake. The BLIMP moves forward at nearly the same speed as the boat to which it is tethered and takes images every 5 s, resulting in more than 90% overlap between sequential frames. The imagery height was kept at ~400 m, which provided IR images with ~0.8 m pixel resolution. From 11h45 to 16h30, moving at a speed of ~1 ms^{-1}, the ZiviCat covered a ~16 km long and ~500 m wide trajectory. However, only the last 3 h of the campaign showed noticeable LSWT patterns.

In order to demonstrate our methodology for the LSWT image processing, we selected a ~24 min segment, i.e., five FFC intervals, which includes 287 IR frames. Some examples of raw IR images from the selected period are shown in Fig. 3. They only cover a narrow band in the 14-bit output (16,384 grey levels) of the camera (~2550 to 2720 in grey values) because of the low temperature contrast over the field of view of the IR camera. The inter-frame grey value variations, e.g., cold (Frame 1) to warm (Frame 31), or warm (Frame 61) to cold (Frame 91), reveal a clear temporal drift problem. This variation is non-linear in time (shown later), and sometimes it is within the range the frame spatial contrast between two FFC periods (e.g., compare Frames 1 and 31 in Fig. 3). Nonuniformity is also evident in the raw images, e.g., cold corner areas of Frames 1, 121, and 151, or warm corners in Frame 31 (Fig. 3). The main LWST feature, e.g., the elongated cold streak in the middle of Frame 1 disappears in Frame 181, because the platform is moving during the thermal imagery recording. This can also be seen by following the position of the ZiviCat, indicated by a red dot in the Fig. 3 images, and its track due to water mixing. A similar track was produced by the accompanying boat navigating "below" the ZiviCat (more evident in Frames 1 and 181). This movement of the platforms requires that consecutive images be assembled along the track of the BLIMP. We implemented an image processing procedure that combines available methods to address and correct all these issues for LSWT image registration.

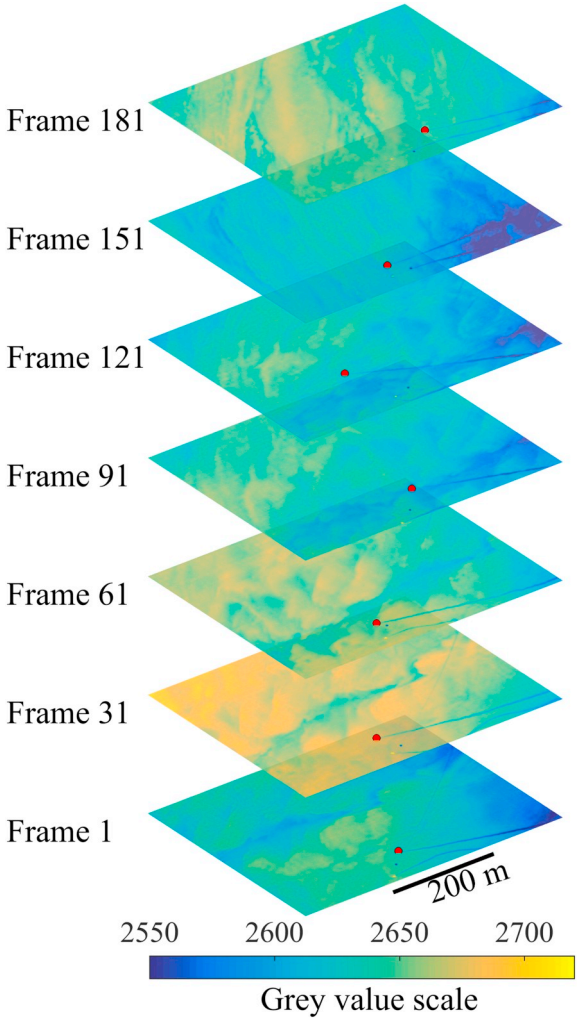

Fig. 3. Examples of 7 selected raw infrared (IR) images 30 frames apart (collected on 18 March 2016) with a pixel resolution of ~0.8 m and a frequency of 0.2 frames per second (FPS). The color map shows the IR camera output as grey values (given in the legend). A red dot indicates the position of the ZiviCat in each frame. This figure illustrates both spatial (e.g., more pronounced in Frame 151) and temporal (e.g., grey value variation between Frames 1 and 31) noise of the thermal images. The change of the surface pattern structures among the frames is due to the moving BLIMP (e.g., take the catamaran position as a reference point to visualize the movement). (For interpretation of the references to color in this figure legend, the reader is referred to the web version of this article.)

2.3. Image enhancement, registration and calibration procedure

The procedure we developed to estimate and correct noise in the images, register all the images, and calibrate them is shown in Fig. 4. It consists of three main steps: (i) pre-processing, (ii) image registration, and (iii) and post-processing.

In the pre-processing step, we first read the raw 14-bit thermal images collected during the field measurements. A spatial filter, e.g., Gaussian filter or median filter, is then applied to reduce the salt-and-pepper noise evident in raw thermal images (Vollmer and Möllmann, 2011). The filter size, i.e., the standard deviation value (Gaussian filter) or the radius (median filter), was selected so as to retain the sub-pixel scale patterns of the LSWTs. In the next step, a preliminary NUC investigation is carried out. For this, FLIR camera images of a ~1.5 × 1.5 m metal plate were recorded under low (controlled cold room at ~4 °C) and high (night-time windowless basement room at ~25 °C with minimum airflow) temperatures. A NUC is then performed on these images following the two-point algorithm of Budzier and Gerlach (2015). In this approach, the deviation in pixel ij, ΔU_{ij}, from the mean scene value, $\langle U \rangle$, is a linear function of the pixel value:

$$\Delta U_{ij} = U_{ij} - \langle U \rangle = a_{ij} U_{ij} + b_{ij} \quad (1)$$

where U_{ij} denotes the pixel grey value of pixel ij. We used 500 frames under constant low and high temperature conditions for this calibration, and so obtained the linear regression model parameters, a and b in Eq. (1), for each pixel (given in Fig. S1a and b in the Supplementary Materials (SM) section). The linear model had mean and maximum residuals of 1.9 and 4.5 in grey value, respectively (Fig. S1d in SM). Afterwards, the pixel value corrected for nonuniformity is calculated by subtracting the deviation, Eq. (1), from the measured irradiance of each frame:

$$U^k_{ij,NUC} = U^k_{ij} - \Delta U^k_{ij} = (1 - a_{ij}) U^k_{ij} - b_{ij} \quad (2)$$

where k is the frame number. An example of the NUC operation on the field data is shown in Fig. 5. It reveals that the preliminary NUC enhances the thermal imagery (e.g., the enhancement of the top-right cold corner and the central warm area of the image). The corresponding

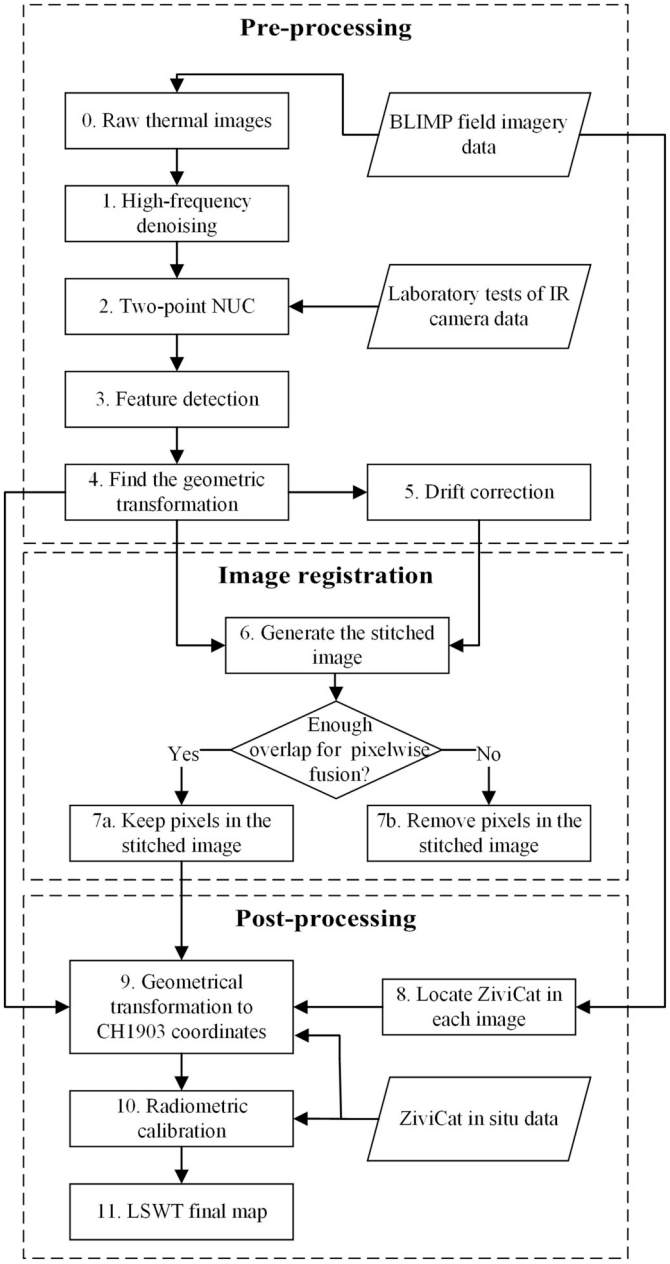

Fig. 4. Flowchart of the procedure for image enhancement (top), registration (center) and calibration (bottom).

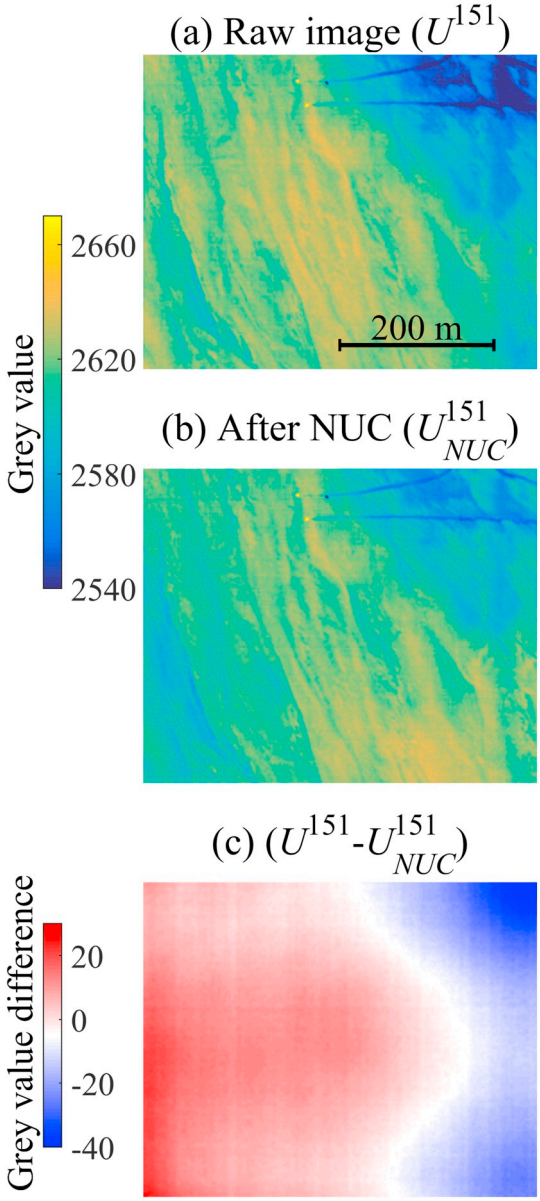

Fig. 5. An example of NonUniformity Correction (NUC) of Lake Geneva thermal imagery: (a) raw thermal image (Frame 151 of the selected images in Fig. 3, 640 × 512 pixels) with a pixel resolution of ~0.8 m, (b) the image after NUC, and (c) the difference between (a) and (b). Note that the grey value range of the legend in (a) and (b) is different than that of panel (c) and also of Fig. 3.

NUC in grey value (Fig. 5c) indicates that the nonuniformity errors over inland water bodies can be comparable with the frame contrast at the given scales (range of color map in Fig. 5a and b). However, examining the NUC method under lower contrast conditions, e.g., in wintertime when spatial LSWT variation is minimal, reveals that some artifacts still remain in the images (not shown here). This can be due to the very low temperature contrast of LSWTs, environmental conditions different from the laboratory tests (especially humidity and higher sensor-environment temperature difference), errors associated with the parameter estimations, or the linearity assumption in the two-point NUC algorithm. In the present investigation, the large overlap area between subsequent images permits further improvement of the nonuniformity effect (Section 3).

Compared to aircraft systems, tilting was expected to be negligible with the BLIMP Picavet rigging system. Therefore, an image with minimal (close to zero) Inertial Measurement Unit (IMU) values (negligible tilting) was selected as a first image. After applying the preliminary NUC to all selected images, the geometric transformation of the images with respect to the first image was calculated. To do this, a feature detection and matching technique was applied. Since strong sub-pixel scale features (~1 m image resolution) are not likely over natural waters, we combined the Speeded-Up Robust Features (SURF) (Bay et al., 2008) and Maximally Stable Extremal Regions (MSER) (Matas et al., 2004) algorithms for feature detection in each frame. An example of features found by the SURF and MSER algorithms is shown in the SM section (Fig. S2). The matching of the points between two frames and their relative geometrical transformation was obtained using the Maximum Likelihood Estimation SAmple Consensus (MLESAC) (Torr and Zisserman, 2000) algorithm. We applied an affine transformation, which preserves straight lines and planes. The above mentioned algorithms require that certain parameters be specified. These were selected such that the final stitched image keeps the main patterns over the lake (by eye inspection). More importantly, an

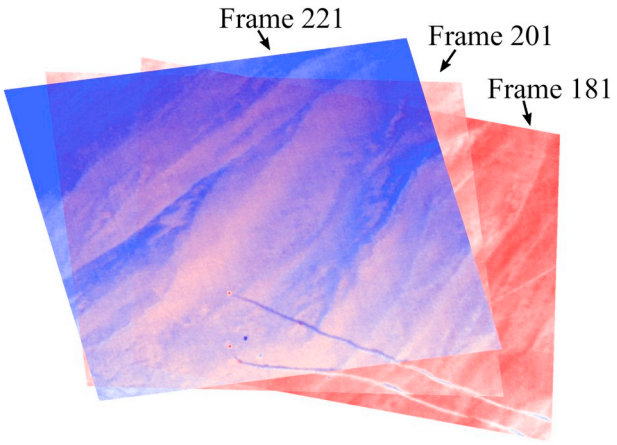

Fig. 6. An example demonstrating the performance of the feature-based image registration algorithm. It shows Frames 181, 201 and 221 (after the NUC was applied) overlaid, based on matched features. Here we selected one image every 20 frames only for visualization purposes; a much higher amount of overlap exists between consecutive images. Note that, for example, the ZiviCat and the accompanying boat tracks appear twice to show the motion between the first two images (bottom) and then between all three images.

objective metric was used, i.e., that the irradiance values match well the in situ temperature data measured by the ZiviCat (discussed below in Section 3). All image processing in this study, including the subroutines for feature detection and estimation of the geometrical transformation, were written in Matlab (last accessed 25 October 2018). An example of three overlaid frames (20 frames apart; Fig. 6) demonstrates the excellent performance of the selected methods and parameters in preserving the main LSWT features in the stitched image (see the two boat tracks in the lower parts, or the streak-like features in the middle of Fig. 6). The change of inter-frame grey values is due to drift and will be discussed below.

As mentioned earlier, uncooled IR cameras suffer from shutter-based drift. Two examples, in Figs. 3 and 6, illustrate this problem for LSWT thermography. Even though the FLIR camera implements the internal FFC every ~5 min, drift is still evident within each FFC interval and is seen as an increase or decrease of the grey value from frame-to-frame. To correct this internal grey value variation that is non-physical with respect to LSWTs, the overlapped areas between consecutive pairs of frames were found using the geometric transfer functions obtained above. We then estimated and matched the probability distribution of the grey values for the overlapped area of each frame. The matching was achieved by computing the cross-correlation of the overlapped areas, finding the lag in the grey value distribution, and subsequently shifting the level of the second image to the first one. Thereafter, the corrected second image was used to correct the third image, and so on. In other words, the shutter-based drift corrected pixel value, $U_{ij,\ Sh}^{k}$, is estimated as:

$$U_{ij,Sh}^{k} = U_{ij,NUC}^{k} + c_k = (1 - a_{ij})U_{ij}^{k} - b_{ij} + c_k \tag{3}$$

where c_k is the drift correction associated with frame number k, and is calculated as follows:

$$P(U_{ij,NUC}^{k} + c_k)_{OL} \cong P(U_{ij,Sh}^{k-1})_{OL} \tag{4}$$

Here, P denotes the estimate of the Probability Distribution Function (PDF), and OL is the overlapped area. In this methodology, the drift correction for the first frame, for which we take the frame right after the FFC, is zero ($c_1 = 0$). We also tested correcting the drift by using the spatially averaged values of the overlapped area. However, errors cumulated through the image sequence and the results (not shown) were less satisfactory than those of the present methodology. Fig. 7a gives an example of the drift problem, and its correction

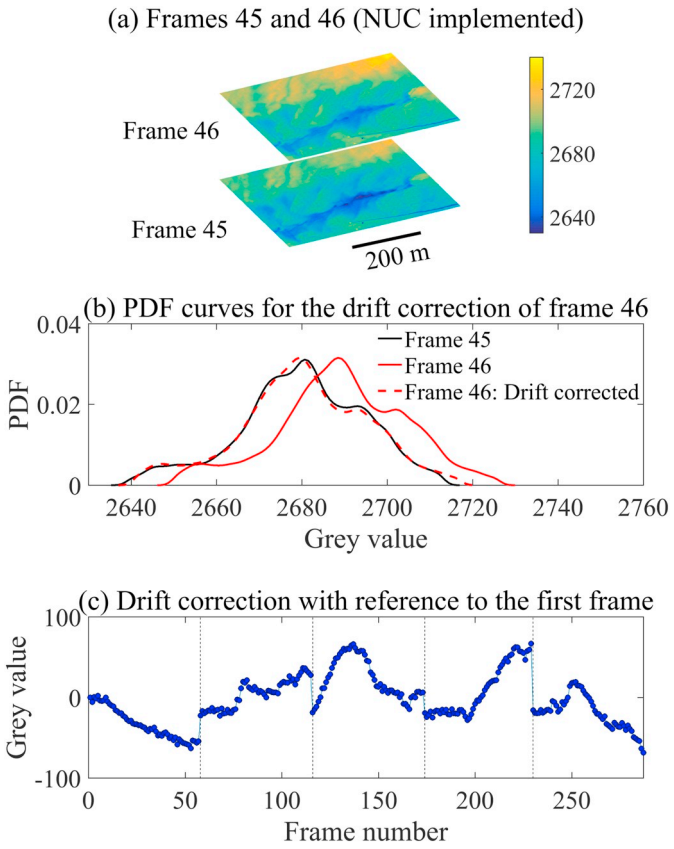

Fig. 7. (a) An example of drift problems in thermal imagery. Note the evidently non-physical increase of grey values from Frame 45 to Frame 46 (see color bar for grey value), (b) The Probability Distribution Function (PDF) of Frames 45 and 46 (solid lines), together with the PDF of the drift-corrected Frame 46 (dashed line). The corresponding correction obtained by the cross-correlation analysis is found to be ~9.1 in grey value, and (c) The drift correction for the entire selected frame series with respect to the first frame. FFC periods are indicated by dashed-vertical lines.

procedure is illustrated in Fig. 7b. The drift correction for the whole frame sequence (287 frames in five FFC periods) is presented in Fig. 7c. The results suggest that the drift problem is non-linear between and within FFC intervals.

After the pre-processing step, all the selected images were registered. Image stitching was accomplished using the geometrical transform functions obtained through feature detection and matching in the pre-processing step. Pixelwise image fusion was performed to create the composite image. Although there are various methods for image fusion (Anita and Moses, 2013), here we used simple averaging to fuse a set of input intensities at each pixel:

$$U_{pq,reg} = \frac{\sum_{m \in \{k_{pq,reg}\}} U_{pq,Sh}^{m}}{N_{pq,reg}} \tag{5}$$

where $U_{pq,\ reg}$ is the intensity value at location pq of the composite image and $N_{pq,\ reg}$ is the number of frames that are included in the calculation of the mean overlapped grey value at pq, i.e., $\{k_{pq,\ reg}\}$. Thereafter, a statistical criterion using the number of overlapped pixels was applied to keep a pixel in the stitched image or to remove it. This is based on the statistical variation of the grey value as a function of N_{OL}, i.e., the number of overlapped images at each pixel. Results will be given in Section 3. At the end of this step, the overall corrected LSWT thermal image in grey values is established. However, two more steps are required: (i) mapping the obtained pattern into geographic coordinates to correlate the BLIMP data to the ZiviCat data, and (ii)

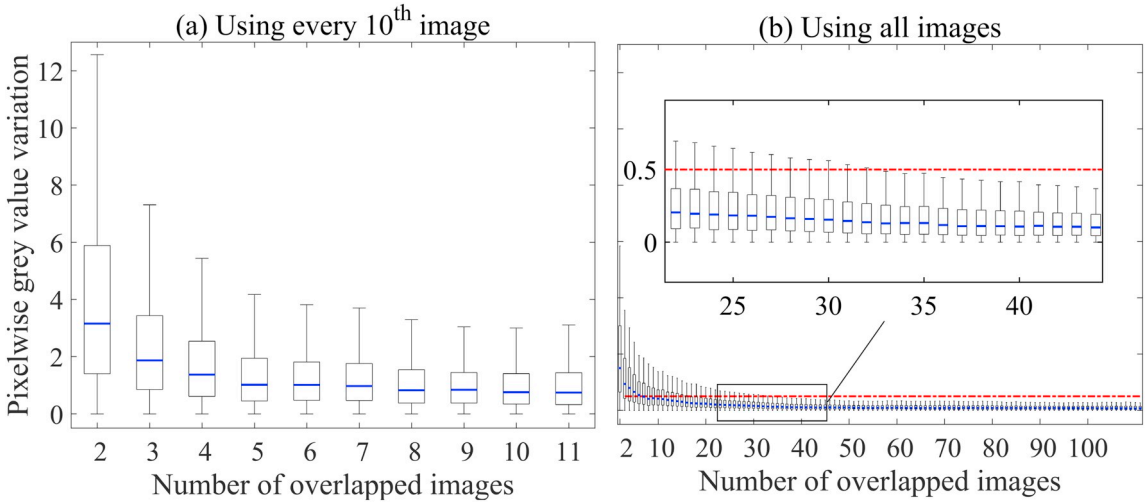

Fig. 8. Pixelwise grey value variation as a function of the number of overlapped images obtained by using (a) every 10th image, and (b) all images. The typical value (median, blue lines), the likely range of variation (interquartile, black boxes) and the wider range of variation (whiskers extent, solid black lines) excluding outliers are given in the box plots. The red line in (b) corresponds to 0.5 grey value variation that is used as an arbitrary threshold here. Inset: zoom on the interval of number of overlapped images where the chosen threshold intersects the maximum grey value variation. (For interpretation of the references to color in this figure legend, the reader is referred to the web version of this article.)

converting grey values to temperatures by carrying out the radiometric calibration to produce the temperature map.

For both of these steps (post-processing in Fig. 4), the ZiviCat in situ measurements are needed. First, the ZiviCat location in each image has to be found. Solid objects, i.e., ZiviCat and the boat, usually produce pixels with the highest intensity (for example, see hot spots in Figs. 5 and 6). Due to the high overlap ratio between consecutive images (~95%), the displacement of objects is expected to be small between sequential frames. Therefore, the ZiviCat is manually located in the first image. In order to locate the ZiviCat in the second image, we search for the pixel with the highest intensity within a small radius, i.e., ~20 pixels, around that pixel. We repeated the same procedure for the following frames always using the ZiviCat location in the previous frame (see examples in Fig. 3 shown by red dots). Using these locations, together with the geometric transformation for each frame from the pre-processing step, ZiviCat locations are pinpointed on the stitched image. Since BLIMP and ZiviCat have separate data acquisition systems, the meta-data synchronization was accomplished through time matching. The corresponding GPS coordinates, recorded by the ZiviCat, permitted transforming the final stitched image from pixel coordinates to the geographic coordinates.

Conversion of pixel grey values to actual temperatures was achieved through radiometric calibration by using (Horny, 2003):

$$T_{pq,zc} = \frac{B}{\ln[R/(U_{pq,reg} - O) + F]} \tag{6}$$

where B, R, O and F are the calibration coefficients that were determined through a non-linear regression analysis. The close-to-the-surface (2 cm depth) in situ temperatures measured by ZiviCat, $T_{pq,\,zc}$, and the corresponding grey values in the stitched image, $U_{pq,\,reg}$, were used to find these parameters. Prior to that, the actual depths of the ten *RBRsolo* thermistors (Fig. 2c) due to the ZiviCat frame movement were corrected by employing the ZiviCat IMU data. Finally, the LSWT map was obtained from the grey values of the stitched images with Eq. (6).

3. Results and discussion

In this section, we show results for the selected IR frame series over Lake Geneva in order to illustrate the performance of the proposed procedure for LSWT image registration and calibration. The thermal map obtained with full correction will be presented, and compared with the maps without NUC, without drift correction, or using fewer frames for image fusion to demonstrate the effect of each of the main steps of image processing, i.e., NUC, drift correction and image fusion.

To examine the effect of the pixelwise averaging on the image registration (image fusion), the results using all images (0.2 FPS, and an average of ~95% overlap between consecutive images) were compared with the thermal map considering only every 10th image (0.02 FPS, and an average of ~86% overlap between consecutive images). When using only every 10th image, the current algorithm of feature detection and estimation of the geometric transformation failed (results not shown). This is apparently due to lack of enough features, and also the significant movement of the catamaran ZiviCat and the accompanying boat (moving objects) between frames in the 10th image configuration. Therefore, we employed the geometrical transformations corresponding to the subset of images, i.e., every 10th image, computed using all images. According to the preliminary results, a higher number of overlapped images for a pixel results in a higher enhancement on the stitched image. For example, the edges of the stitched image, where the number of overlapped images is lower, show more non-physical spatial variability. To quantify the effect of smoothing by image fusion, and consequently to find a criterion for omitting the pixels with insufficient overlaps, we calculated the variation of the grey value, $(\Delta U)_{N_{OL}}$, as a function of the number of overlaps, N_{OL}, at each pixel:

$$(\Delta U_{pq,reg})_{N_{OL}} = |(U_{pq,reg})_{N_{OL}} - (U_{pq,reg})_{N_{OL}-1}| \tag{7}$$

According to Eq. (7), at an arbitrary position, pq, on the registered image, the variation due to N_{OL} overlaps is defined as the change of the absolute grey value resulting from adding a new frame which includes pq to the registered image, i.e., using Eq. (5). This variation may change with location on the registered image. Therefore, we calculated the statistical parameters of variation as a function of the number of overlapped images. Fig. S3 in the SM presents the maps of the number of overlaps for both cases studied, using every 10th image and using all images.

The median and the range of grey value variations for each number of overlapped images were then calculated and were presented as box plots (Fig. 8). It is evident that using more overlaps leads to less pixelwise grey value variation. Here, the results of Fig. 8a at point 3 on the x-axis, should be compared with the corresponding results in Fig. 8b at point 30 on the x-axis. In this example, point 3 in Fig. 8a showed a median and maximum variation of ~2 and 7, respectively, and for the

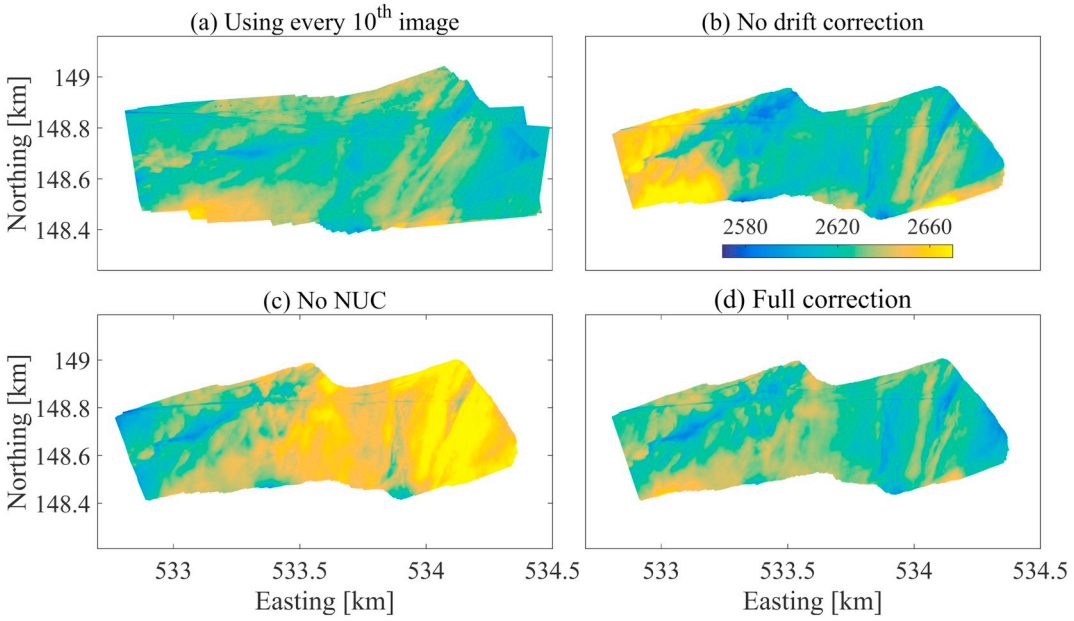

Fig. 9. Surface thermal maps of a section of Lake Geneva in grey value (step 9 in Fig. 4) obtained by: (a) Using every 10th image (to examine the effect of step 7 in Fig. 4), (b) Neglecting the drift correction (to examine the effect of step 5 in Fig. 4), (c) Neglecting NUC (to examine the effect of step 2 in Fig. 4), and (d) with full correction. Legend in (b) indicates the grey value scale valid for all panels.

corresponding point in Fig. 8b (point 30), a median and maximum variation of ~0.2 and 0.6, respectively, were found.

The results of Fig. 8b can also be used to define a threshold for the number of overlaps in the stitched image. In this study, we considered a threshold of 35 frames for image fusion, i.e., $N_{cr,\ OL} = 35$ in step 7 of Fig. 4. This point is at the beginning of the flat part of the curve in Fig. 8b, and has an average maximum variation of < 0.5 grey value (as indicated by the red line in Fig. 8b). We applied this criterion to generate the final thermal maps shown below.

After BLIMP-ZiviCat time synchronization, as explained above, the catamaran pixel-GPS locations were used to create the final thermal map in CH1903 Swisstopo coordinates (last accessed 25 October 2018). In order to reveal the effectiveness of the proposed image processing procedure, the results are given (Fig. 9) for full correction in all images, as well as the thermal maps without implementing NUC, without drift correction, and using fewer frames for image fusion. The results confirm that the high-frequency denoising (step 1 in Fig. 4) preserved the main features of the thermal images. For this operation, we implemented both the median and Gaussian filters. The difference between the two resulting thermal maps was insignificant at the given scale (we only show the results applying the Gaussian filter).

Using fewer frames for image fusion (Fig. 9a) produces less image contrast difference compared to the full correction map (Fig. 9d), and the resulting map is not satisfactory in terms of preserving all or even the main features in the stitched image. For example, the IR boat tracks are not as clear as in Fig. 9d. In addition, due to the lack of sufficient frames for image fusion (as also shown in Fig. 8), some artifacts are evident in the areas with less overlaps (e.g., close to the edges of Fig. 9a). Furthermore, the geometrical transformation to CH1903 coordinates is slightly tilted compared to using full images (Fig. 9d). This, again, is due to the insufficient number of frames needed for the transformation. Although lower overlap ratios of > 75% for image registration of low contrast scenes without spatiotemporal noise (e.g., Ramli et al., 2017) and > 50% for IR images with higher contrast and more features (e.g., Kim and Lee, 2013) were suggested, our results indicate that a higher overlap (~95% in this case) is essential for proper image registration over inland waters with low contrast using an uncooled IR camera.

Fig. 9 also indicates that neglecting NUC or the drift correction can cause non-physical spatial gradients over the stitched image (e.g., note the warm areas in Figs. 9b and c). The warm areas in the left part of Fig. 9b result from the negative drift correction required for the first FFC interval (Fig. 7c), whereas in the center parts, the averaging due to a high number of overlaps (Fig. S3 in SM) compensates the drift problem. Fig. 9c illustrates a gradual warming from the left (first frame) to the right (last frame) of the stitched image. This is due to the recursive behavior of the drift correction methodology. This methodology uses the PDF matching between overlapped areas of consecutive frames, but then applies the obtained correction to the whole frame. NUC is particularly effective on the edges (see Fig. 5c as an example), which mainly contain the non-overlapped regions of the frame. Therefore, neglecting NUC retains an error in a frame for the subsequent drift correction. This error is cumulative over subsequent frames, causing warming in this case. To confirm this, we generated a stitched image neglecting both NUC and drift correction (Fig. S4 in SM). It shows a map similar to Fig. 9b (no drift correction) with more artifacts on the edges due to omitting NUC.

To further investigate the performance of the procedure, the matching of the measured in situ near-surface temperatures (at about 2-cm depth) with the corresponding grey value on the stitched image is required. However, the in situ measured temperatures are affected by the ZiviCat track in the stitched image. Since the ZiviCat moves forward, the mixing caused by the propellers at the back of the catamaran contaminates the previous in situ measurement points (downstream of the catamaran) in the thermal map (obvious in LSWT images, particularly in Figs. 5, 6 and 9). Therefore, the corresponding irradiance values at the ZiviCat measurement pixels cannot be used for the radiometric calibration. An alternative would be to use the grey values of the uncontaminated pixels in front of the ZiviCat track, together with the corresponding temperatures (ahead in time). However, image fusion is essential for thermal image registration over water (Figs. 8 and 9a) and usually there are not enough pixels (< 10) available for this analysis. The LSWT temperature range is likely to be too small over such a short distance, as in the present case, and a proper radiometric calibration cannot be carried out either.

In order to overcome these problems, the average grey values at ~3 m to the left and the right of the actual ZiviCat track, i.e., 4 pixels to the left and the right of the in situ measurement points, were used

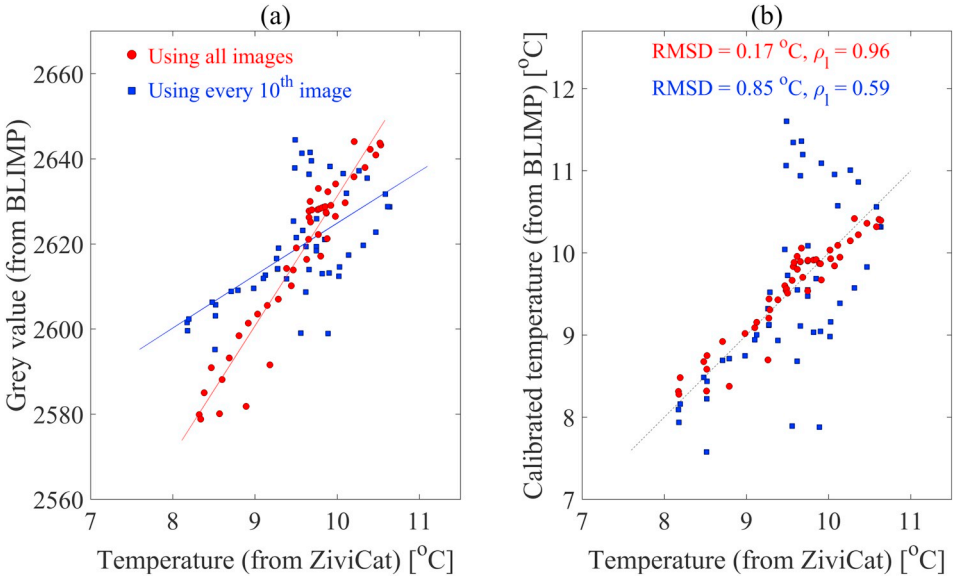

Fig. 10. (a) Comparison of the grey value of the stitched image (from the airborne BLIMP) with the corresponding in situ near-surface (2 cm depth) temperatures measured by the catamaran ZiviCat using every 10th image (blue squares) and all images (red circles). The solid lines show the corresponding radiometric calibrations, Eq. (6), which tend to be linear for a narrow temperature range (< 3 °C); and (b) Comparison of ZiviCat temperatures with those obtained from the radiometric calibration of the BLIMP grey scales for the same two overlap cases as in panel (a). The dotted line indicates the identity (1:1) line. The RMSDs for the non-linear regression model, and the correlation coefficients, ρ_l, for a linear curve fitting are given in the legend of (b). (For interpretation of the references to color in this figure legend, the reader is referred to the web version of this article.)

instead for the irradiance-to-temperature conversion in the present analysis. To minimize errors due to this assumption, areas with minimal grey value differences between pixels to the left and the right of the ZiviCat track should be selected. Furthermore, to cover wider temperature ranges, regions with higher along-track spatial variability are preferable. Considering these requirements, the along-track measurement frames between 533.95 and 534.3 km in Fig. 9d were selected (50 frames with their locations shown in Fig. S5 in SM). The comparison between the measured temperatures (from ZiviCat) and the enhanced grey values (processed BLIMP data) for the thermal maps of Figs. 9a and d are shown in Fig. 10a. It again demonstrates the poor performance when using fewer frames for image stitching and fusion and it indicates a relatively low RMSD and high correlation coefficient when using the proposed method for the whole image registration (Fig. 10b). The observed deviations between the grey values and LSWTs (red circles in Fig. 10a) can be due to errors in the estimation of the geometric transformations, the difference between skin (top 10–500 μm layer) and near-surface temperatures (Minnett et al., 2011; Wilson et al., 2013), uncertainties in the ZiviCat measured and corrected data, and errors induced by averaging above/below pixels for the comparison.

In the last step of this procedure, the radiometric calibration (step 10 in Fig. 4) is required to convert the obtained grey value thermal map (Fig. 9d) into a temperature map. A non-linear regression analysis following an ordinary least-square approach was carried out to find the best-fit parameters in Eq. (6). The solid lines in Fig. 10a show the fitted curves. We note that Eq. (5) was developed for a wide range of temperatures (> 50 °C), as confirmed by the wide range of confidence intervals obtained for the estimated calibration parameters (not shown here). For a low-contrast scene, a linear relationship is expected and linearity within the < 3 °C range of LSWTs is evident in Fig. 10a. The red solid line parameterization in Fig. 10a was used to convert grey scales into temperature. Results (Fig. 10b) again indicate that a high overlap ratio is needed to obtain reliable temperatures. These conversions were used to construct the sub-pixel scale thermal map (Fig. 11 with ~0.8 m resolution) over a section of Lake Geneva. The area covered in Fig. 11, i.e., ~0.61 km^2, resolves less than a typical satellite pixel (1 km^2). However, it shows various cold-warm patches and long streak-like structures on the lake surface with a temperature contrast of > 2 °C, which are not resolved in satellite images.

Past studies have examined sub-pixel scale surface temperature variability by using airborne systems. However, due to the challenges intrinsic to thermal image registration over water or instrumental restrictions as explained above, they only reported along-track point

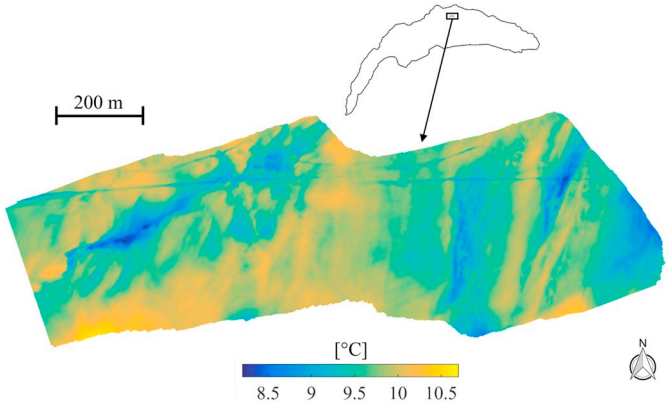

Fig. 11. Lake Surface Water Temperature (LSWT) map at sub-pixel satellite scale over a section of Lake Geneva obtained from aerial remote sensing (see Fig. 2 for measurement platforms) on 18 March 2016 at ~15 h30. This map was created using 287 images with a resolution of ~0.8 m, together with an image processing procedure (Fig. 4). Streaks with temperature differences of several degrees are evident. Note the boat track from west to east across the upper part of the image that creates an "artificial" feature. The legend indicates temperature in °C. See Fig. 1 for the location and bathymetry of the lake.

(Mahrt and Khelif, 2010) or area-averaged (Castro et al., 2017) measurements. The developed two-platform measurement system, together with the proposed image processing procedure, can be used to obtain LSWT patterns at sub-pixel scales for systematic studies over larger areas, a wider range of conditions, and at other low-contrast sites. The detailed features that became visible in the map in Fig. 11 can also help improve understanding and estimating mass, heat, and momentum exchanges at the air-water interface (e.g., Rahaghi et al., 2018a). Previously, temporal sub-pixel LSWT variability was observed in point measurements (Vercauteren et al., 2008; Rahaghi et al., 2018b). It is now apparent that this variability may be linked to 2D patterns of narrow streaks that may reach several hundred meters length or patches of variable size and variable LSWT structure.

4. Summary and conclusions

In this study, we presented aerial thermography results over a section of a large lake (Lake Geneva) obtained with a two-platform measurement system consisting of a balloon-launched measurement platform (BLIMP) and an autonomously operating catamaran called ZiviCat

for ground-truthing and radiometric calibration. An uncooled microbolometer camera was used for which spatial noise, i.e., nonuniformity, and temporal drift are intrinsic. It was demonstrated that a procedure for correction and enhancement of the IR images before and throughout the image registration procedure (Fig. 4) is essential for obtaining reliable Lake Surface Water Temperature (LSWT) maps, because LSWTs have much lower contrast than is typically observed in land-based scenes. A preliminary two-point NUC (using laboratory measurements, Fig. 5), together with drift estimation through PDF matching of the overlap regions of consecutive frames (Fig. 7), were implemented prior to image registration. The selected frames were registered to create a stitched image covering a wider area. To estimate the geometric transformations for image registration, the blob and region features were detected applying SURF and MSER techniques (Figs. 6 and S2 in SM). Then, MLESAC was employed to find the transformation functions by matching the combination of these features among frames. Due to a large degree of overlap, a simple averaging was used on the stitched image to fuse the grey value at each pixel.

The results indicated that neglecting either the NUC or the drift correction can produce substantial artificial spatial gradients in the stitched image (Fig. 9b and c). Furthermore, using all images, providing ~95% overlap between consecutive frames, allowed the accurate generation of the stitched image (Figs. 9a and 10), whereas imagery with less overlap, e.g., ~86% overlap, failed. The final result (Figs. 10 and 11) showed the capability of the two-platform measurement system and the proposed image-processing procedure to resolve LSWT patterns at sub-pixel satellite scale over a lake. It was also demonstrated that in such low-contrast moving scene cases containing only a few clearly identifiable mobile objects such as boats, a high overlap ratio (~95% in our case), combined with spatiotemporal noise reduction, is essential for accurate LSWT thermography. This resulted in the generation of sub-pixel scale LSWT maps that revealed spatial LSWT variability with unprecedented detail.

The proposed image processing procedure is a tool that can be applied to any comparable data set, if the LSWTs have sufficient contrast (discussed in Section 3) and the speed of movement of the two-platform measurement system allows for a sufficiently high overlap ratio of the thermal images.

Calibrated high-resolution airborne thermography of LSWTs at sub-pixel scale, as discussed in this paper, is a technique that can open up new ways to investigate various aspects of lake research, since thermal conditions at the surface determine many factors affecting lake ecosystem functioning as a whole. The obtained maps reveal 2D LSWT structures never seen before with such a resolution. They consist of narrow streaks that may be hundreds of meters long and coherent patches characterized by variable size and temperature gradients. These features may challenge present physical limnological concepts, in particular, those dealing with the air-water exchange dynamics of mass, heat and momentum at the sub-pixel scales (~1 m resolution). This, in turn, will affect the subtleties of biological, chemical and geological processes in the lake, because the pattern of streaks and patches with strong horizontal temperature gradient as seen in Fig. 11, indicates that an important vertical exchange between different layers in the upper layers of the lake is taking place on horizontal scales of only several meters. Visualizing LSWT details through calibrated airborne thermography can also be helpful in dedicated studies of river inflows, wastewater discharges and near-shore processes, e.g., thermal biomes and their spreading in the lake, all of which will affect the lake ecosystem dynamics. LSWT maps provide suitable data for ground-truthing and spatial downscaling of satellite data and can improve the prediction results of numerical weather models for which air-water exchange processes are an important input. And finally, it is of interest to note that the present campaign took approximately 5 h to cover an area of approximately 8 km^2 and thus, an entire lake surface survey could be carried out in a single day in a smaller lake.

Acknowledgements

This work was supported by the Fondation pour l'Etude des Eaux du Léman (FEEL), Lausanne, Switzerland [grant number 5257]. The authors would like to thank J.-L. Liardon, H.K. Wynn, P.O. Paccaud, B. Geissmann, L. Zulliger, J. Béguin, P. Klaus, N. Gujja Shaik, S. Benketaf, K. Kangur, M. Pagnamenta, L. Hostettler, N. Bongard, G. Ulrich, B. Grossniklaus, A. Rosselet, M. Bolay, J. Rossier, Y. Poffet and N. Roussel for their contribution to designing, testing, and improving of the BLIMP and ZiviCat platforms used in this research. We also wish to thank A. Ivanov and S. Tulyakov for their help and advice on BLIMP image processing. We thank the reviewers for their constructive comments and suggestions that helped improve the paper.

Appendix A. Supplementary Materials

Supplementary data to this article can be found online at https://doi.org/10.1016/j.rse.2018.12.018.

References

Adrian, R., O'Reilly, C.M., Zagarese, H., Baines, S.B., Hessen, D.O., Keller, W., Livingstone, D.M., Sommaruga, R., Straile, D., Van Donk, E., Weyhenmeyer, G.A., Winder, M., 2009. Lakes as sentinels of climate change. Limnol. Oceanogr. 54, 2283–2297. https://doi.org/10.4319/lo.2009.54.6_part_2.2283.

Anita, S.J.N., Moses, C.J., 2013. Survey on pixel level image fusion techniques. In: 2013 IEEE International Conference on Emerging Trends in Computing, Communication and Nanotechnology (ICECCN 2013). IEEE, Tirunelveli, India, pp. 141–145. https://doi.org/10.1109/ICE-CCN.2013.6528480.

Balsamo, G., Salgado, R., Dutra, E., Boussetta, S., Stockdale, T., Potes, M., 2012. On the contribution of lakes in predicting near-surface temperature in a global weather forecasting model. Tellus Ser. A 64, 15829. https://doi.org/10.3402/Tellusa.V64i0.15829.

Barry, D.A., Liardon, J.-L., Paccaud, P., Klaus, P., Gujja Shaik, N.S., Rahaghi, A.I., Zulliger, L., Beguin, J., Geissmann, B., Tulyakov, S., Ivanov, A., Wynn, H.K., Lemmin, U., 2018. A low-cost, autonomous mobile platform for limnological investigations, supported by high-resolution mesoscale airborne imagery. PLoS One (Submitted).

Bauersachs, T., Rochelmeier, J., Schwark, L., 2015. Seasonal lake surface water temperature trends reflected by heterocyst glycolipid-based molecular thermometers. Biogeosciences 12, 3741–3751. https://doi.org/10.5194/bg-12-3741-2015.

Bay, H., Ess, A., Tuytelaars, T., Van Gool, L., 2008. Speeded-Up Robust Features (SURF). Comput. Vis. Image Underst. 110, 346–359. https://doi.org/10.1016/j.cviu.2007.09.014.

Beaulieu, M., Pick, F., Gregory-Eaves, I., 2013. Nutrients and water temperature are significant predictors of cyanobacterial biomass in a 1147 lakes data set. Limnol. Oceanogr. 58, 1736–1746. https://doi.org/10.4319/lo.2013.58.5.1736.

Binding, C.E., Greenberg, T.A., McCullough, G., Watson, S.B., Page, E., 2018. An analysis of satellite-derived chlorophyll and algal bloom indices on Lake Winnipeg. J. Great Lakes Res. 44, 436–446. https://doi.org/10.1016/j.jglr.2018.04.001.

Bonvin, F., Razmi, A.M., Barry, D.A., Kohn, T., 2013. Micropollutant dynamics in Vidy Bay-A coupled hydrodynamic-photolysis model to assess the spatial extent of ecotoxicological risk. Environ. Sci. Technol. 47, 9207–9216. https://doi.org/10.1021/es401294c.

Budzier, H., Gerlach, G., 2015. Calibration of uncooled thermal infrared cameras. J. Sens. Sens. Syst. 4, 187–197. https://doi.org/10.5194/jsss-4-187-2015.

Castro, S.L., Emery, W.J., Wick, G.A., Tandy, W., 2017. Submesoscale sea surface temperature variability from UAV and satellite measurements. Remote Sens. 9, 1089. https://doi.org/10.3390/Rs9111089.

Dörnhöfer, K., Oppelt, N., 2016. Remote sensing for lake research and monitoring – recent advances. Ecol. Indic. 64, 105–122. https://doi.org/10.1016/j.ecolind.2015.12.009.

Emery, W.J., Good, W.S., Tandy, W., Izaguirre, M.A., Minnett, P.J., 2014. A microbolometer airborne calibrated infrared radiometer: The Ball Experimental Sea Surface Temperature (BESST) radiometer. IEEE Trans. Geosci. Remote Sens. 52, 7775–7781. https://doi.org/10.1109/Tgrs.2014.2318683.

Ferri, R., Pierdicca, N., Talice, S., 2000. Mapping sea surface temperature from aircraft using a multi-angle technique: An experiment over the Orbetello lagoon. Int. J. Remote Sens. 21, 3003–3024. https://doi.org/10.1080/01431160050144929.

Handcock, R.N., Gillespie, A.R., Cherkauer, K.A., Kay, J.E., Burges, S.J., Kampf, S.K., 2006. Accuracy and uncertainty of thermal-infrared remote sensing of stream temperatures at multiple spatial scales. Remote Sens. Environ. 100, 427–440. https://doi.org/10.1016/j.rse.2005.07.007.

Haselwimmer, C., Prakash, A., Holdmann, G., 2013. Quantifying the heat flux and outflow rate of hot springs using airborne thermal imagery: Case study from Pilgrim Hot Springs, Alaska. Remote Sens. Environ. 136, 37–46. https://doi.org/10.1016/j.rse.2013.04.008.

Hernandez, P.A., Calvari, S., Ramos, A., Perez, N.M., Marquez, A., Quevedo, R., Barrancos, J., Padron, E., Padilla, G.D., Lopez, D., Santana, A.R., Melian, G.V., Dionis, S., Rodriguez, F., Calvo, D., Spampinato, L., 2014. Magma emission rates from shallow submarine eruptions using airborne thermal imaging. Remote Sens. Environ.

154, 219–225. https://doi.org/10.1016/j.rse.2014.08.027.
Horny, N., 2003. FPA camera standardisation. Infrared Phys. Technol. 44, 109–119. https://doi.org/10.1016/S1350-4495(02)00183-4.
Kim, D.S., Lee, K.H., 2013. Segment-based region of interest generation for pedestrian detection in far-infrared images. Infrared Phys. Technol. 61, 120–128. https://doi.org/10.1016/j.infrared.2013.08.001.
Kruse, P.W., 1997. Uncooled infrared imaging arrays and systems. Academic Press, San Diegohttps://www.elsevier.com/books/uncooled-infrared-imaging-arrays-and-systems/willardson/978-0-12-752155-8.
Lahiri, B.B., Bagavathiappan, S., Jayakumar, T., Philip, J., 2012. Medical applications of infrared thermography: A review. Infrared Phys. Technol. 55, 221–235. https://doi.org/10.1016/j.infrared.2012.03.007.
Le Moigne, P., Colin, J., Decharme, B., 2016. Impact of lake surface temperatures simulated by the FLake scheme in the CNRM-CM5 climate model. Tellus Ser. A 68, 31274. https://doi.org/10.3402/Tellusa.V68.31274.
Lemmin, U., Amouroux, A., 2013. The influence of climate change on Lake Geneva. In: Goldman, C.R., Kumagai, M., Robarts, R.D. (Eds.), Climatic Change and Global Warming of Inland Waters. John Wiley & Sons, Chichester, UK, pp. 201–217. https://doi.org/10.1002/9781118470596.ch12.
Lemmin, U., D'Adamo, N., 1996. Summertime winds and direct cyclonic circulation: Observations from Lake Geneva. Ann. Geophys. Ser. A 14, 1207–1220. https://doi.org/10.1007/s005850050384.
Liardon, J.-L., Barry, D.A., 2017. Adaptable imaging package for remote vehicles. HardwareX 2, 1–12. https://doi.org/10.1016/j.ohx.2017.04.001.
Liardon, J.-L., Hostettler, L., Zulliger, L., Kangur, K., Shaik, N.G., Barry, D.A., 2017. Lake imaging and monitoring aerial drone. HardwareX 3, 146–159. https://doi.org/10.1016/j.ohx.2017.10.003.
Livingstone, D.M., Dokulil, M.T., 2001. Eighty years of spatially coherent Austrian lake surface temperatures and their relationship to regional air temperature and the North Atlantic Oscillation. Limnol. Oceanogr. 46, 1220–1227. https://doi.org/10.4319/lo.2001.46.5.1220.
Mahrt, L., Khelif, D., 2010. Heat fluxes over weak SST heterogeneity. J. Geophys. Res. Atmos. 115, D11103. https://doi.org/10.1029/2009jd013161.
Marinetti, S., Maldague, X., Prystay, M., 1997. Calibration procedure for focal plane array cameras and noise equivalent material loss for quantitative thermographic NDT. Mater. Eval. 55, 407–412. https://www.osti.gov/scitech/biblio/471095.
Matas, J., Chum, O., Urban, M., Pajdla, T., 2004. Robust wide-baseline stereo from maximally stable extremal regions. Image Vis. Comput. 22, 761–767. https://doi.org/10.1016/j.imavis.2004.02.006.
Mesas-Carrascosa, F.J., Perez-Porras, F., de Larriva, J.E.M., Frau, C.M., Aguera-Vega, F., Carvajal-Ramirez, F., Martinez-Carricondo, P., Garcia-Ferrer, A., 2018. Drift correction of lightweight microbolometer thermal sensors on-board unmanned aerial vehicles. Remote Sens. 10https://doi.org/10.3390/Rs10040615. Artn 615.
Milton, A.F., Barone, F.R., Kruer, M.R., 1985. Influence of nonuniformity on infrared focal plane array performance. Opt. Eng. 24, 855–862. https://doi.org/10.1117/12.7973588.
Minnett, P.J., Smith, M., Ward, B., 2011. Measurements of the oceanic thermal skin effect. Deep-Sea Res. II 58, 861–868. https://doi.org/10.1016/j.dsr2.2010.10.024.
Mounier, E., 2011. Technical and market trends for microbolometers for thermography and night vision. In: Proc SPIE 8012, Infrared Technology and Applications XXXVII (p. 80121u). Orlando, Florida, United States, https://doi.org/10.1117/12.877050.
Neale, C.M.U., Jaworowski, C., Heasler, H., Sivarajan, S., Masih, A., 2016. Hydrothermal monitoring in Yellowstone National Park using airborne thermal infrared remote sensing. Remote Sens. Environ. 184, 628–644. https://doi.org/10.1016/j.rse.2016.04.016.
Nugent, P.W., Shaw, J.A., 2014. Calibration of uncooled LWIR microbolometer imagers to enable long-term field deployment. In: Proc. SPIE 9071, Infrared Imaging Systems: Design, Analysis, Modeling, and Testing XXV (p. 90710v). Baltimore, Maryland, United States, https://doi.org/10.1117/12.2053082.
Nugent, P.W., Shaw, J.A., Pust, N.J., 2013. Correcting for focal-plane-array temperature dependence in microbolometer infrared cameras lacking thermal stabilization. Opt. Eng. 52, 061304. https://doi.org/10.1117/1.Oe.52.6.061304.
Oesch, D.C., Jaquet, J.M., Hauser, A., Wunderle, S., 2005. Lake surface water temperature retrieval using advanced very high resolution radiometer and moderate resolution imaging spectroradiometer data: Validation and feasibility study. J. Geophys. Res. Oceans 110, C12014. https://doi.org/10.1029/2004jc002857.
Oesch, D., Jaquet, J.M., Klaus, R., Schenker, P., 2008. Multi-scale thermal pattern monitoring of a large lake (Lake Geneva) using a multi-sensor approach. Int. J. Remote Sens. 29, 5785–5808. https://doi.org/10.1080/01431160802132786.
O'Reilly, C.M., Sharma, S., Gray, D.K., Hampton, S.E., Read, J.S., Rowley, R.J., Schneider, P., Lenters, J.D., McIntyre, P.B., Kraemer, B.M., Weyhenmeyer, G.A., Straile, D., Dong, B., Adrian, R., Allan, M.G., Anneville, O., Arvola, L., Austin, J., Bailey, J.L., Baron, J.S., Brookes, J.D., de Eyto, E., Dokulil, M.T., Hamilton, D.P., Havens, K., Hetherington, A.L., Higgins, S.N., Hook, S., Izmest'eva, L.R., Joehnk, K.D., Kangur, K., Kasprzak, P., Kumagai, M., Kuusisto, E., Leshkevich, G., Livingstone, D.M., MacIntyre, S., May, L., Melack, J.M., Mueller-Navarra, D.C., Naumenko, M., Noges, P., Noges, T., North, R.P., Plisnier, P.D., Rigosi, A., Rimmer, A., Rogora, M., Rudstam, L.G., Rusak, J.A., Salmaso, N., Samal, N.R., Schindler, D.E., Schladow, S.G., Schmid, M., Schmidt, S.R., Silow, E., Soylu, M.E., Teubner, K., Verburg, P., Voutilainen, A., Watkinson, A., Williamson, C.E., Zhang, G.Q., 2015. Rapid and highly variable warming of lake surface waters around the globe. Geophys. Res. Lett. 42, 10773–10781. https://doi.org/10.1002/2015GL066235.
Parra, F., Meza, P., Toro, C., Torres, S., 2011. Infrared focal plane array imaging system characterization by means of a blackbody radiator. Lect. Notes Comput. Sci 7042, 105–112. https://doi.org/10.1007/978-3-642-25085-9_12.
Perry, D.L., Dereniak, E.L., 1993. Linear-theory of nonuniformity correction in infrared staring sensors. Opt. Eng. 32, 1854–1859. https://doi.org/10.1117/12.145601.
Ptak, M., Choiński, A., Piekarczyk, J., Pryłowski, T., 2017. Applying Landsat satellite thermal images in the analysis of Polish lake temperatures. Pol. J. Environ. Stud. 26, 2159–2165. https://doi.org/10.15244/pjoes/69444.
Rahaghi, A.I., Lemmin, U., Barry, D.A., 2018a. Surface water temperature heterogeneity at sub-pixel satellite scales and its effect on the surface cooling estimates of a large lake: Airborne remote sensing results from Lake Geneva. J. Geophys. Res. Oceans (Submitted).
Rahaghi, A.I., Lemmin, U., Cimatoribus, A., Bouffard, D., Riffler, M., Wunderle, S., Barry, D.A., 2018b. Improving surface heat flux estimation for a large lake through model optimization and two-point calibration: The case of Lake Geneva. Limnol. Oceanogr. Methods 16, 576–593. https://doi.org/10.1002/lom3.10267.
Ramli, R., Idris, M.Y.I., Hasikin, K., Karim, N.K.A., Wahab, A.W.A., Ahmedy, I., Ahmedy, F., Kadri, N.A., Arof, H., 2017. Feature-based retinal image registration using D-Saddle feature. J. Healthc. Eng. 1489524. https://doi.org/10.1155/2017/1489524.
Riffler, M., Lieberherr, G., Wunderle, S., 2015. Lake surface water temperatures of European Alpine lakes (1989–2013) based on the Advanced Very High Resolution Radiometer (AVHRR) 1 km data set. Earth Syst. Sci. Data 7, 1–17. https://doi.org/10.5194/essd-7-1-2015.
Tamborski, J.J., Rogers, A.D., Bokuniewicz, H.J., Cochran, J.K., Young, C.R., 2015. Identification and quantification of diffuse fresh submarine groundwater discharge via airborne thermal infrared remote sensing. Remote Sens. Environ. 171, 202–217. https://doi.org/10.1016/j.rse.2015.10.010.
Tonolla, D., Wolter, C., Ruhtz, T., Tockner, K., 2012. Linking fish assemblages and spatiotemporal thermal heterogeneity in a river-floodplain landscape using high-resolution airborne thermal infrared remote sensing and in-situ measurements. Remote Sens. Environ. 125, 134–146. https://doi.org/10.1016/j.rse.2012.07.014.
Torbick, N., Ziniti, B., Wu, S., Linder, E., 2016. Spatiotemporal lake skin summer temperature trends in the northeast United States. Earth Interact. 20, 1–21. https://doi.org/10.1175/Ei-D-16-0015.1.
Torgersen, C.E., Faux, R.N., McIntosh, B.A., Poage, N.J., Norton, D.J., 2001. Airborne thermal remote sensing for water temperature assessment in rivers and streams. Remote Sens. Environ. 76, 386–398. https://doi.org/10.1016/S0034-4257(01)00186-9.
Torr, P.H.S., Zisserman, A., 2000. MLESAC: A new robust estimator with application to estimating image geometry. Comput. Vis. Image Underst. 78, 138–156. https://doi.org/10.1006/cviu.1999.0832.
Torres, F., Torres, S.N., San Martin, C., 2005. A recursive least square adaptive filter for nonuniformity correction of infrared image sequences. Lect. Notes Comput. Sci 3773, 540–546. https://doi.org/10.1007/11578079_56.
Torres, F., San Martin, C., Torres, S.N., 2006. A RLS filter for nonuniformity and ghosting correction of infrared image sequences. Lect. Notes Comput. Sci 4225, 446–454. https://doi.org/10.1007/11892755_46.
Tozuka, T., Ohishi, S., Cronin, M.F., 2017. A metric for surface heat flux effect on horizontal sea surface temperature gradients. Clim. Dyn. https://doi.org/10.1007/s00382-017-3940-2.
Vercauteren, N., Bou-Zeid, E., Parlange, M.B., Lemmin, U., Huwald, H., Selker, J., Meneveau, C., 2008. Subgrid-scale dynamics of water vapour, heat, and momentum over a lake. Bound.-Layer Meteorol. 128, 205–228. https://doi.org/10.1007/s10546-008-9287-9.
Vollmer, M., Möllmann, K.-P., 2011. Infrared Thermal Imaging: Fundamentals, Research and Applications. Wiley-VCH, Weinheim, Germany. http://eu.wiley.com/WileyCDA/WileyTitle/productCd-3527641556.html.
Williams, T., 2009. Thermal Imaging Cameras: Characteristics and Performance. CRC Press, Boca Raton, USA. https://www.crcpress.com/Thermal-Imaging-Cameras-Characteristics-and-Performance/Williams/p/book/9781420071856.
Wilson, R.C., Hook, S.J., Schneider, P., Schladow, S.G., 2013. Skin and bulk temperature difference at Lake Tahoe: a case study on lake skin effect. J. Geophys. Res. Atmos. 118, 10332–10346. https://doi.org/10.1002/Jgrd.50786.
Woolway, R.I., Merchant, C.J., 2018. Intralake heterogeneity of thermal responses to climate change: a study of large Northern Hemisphere lakes. J. Geophys. Res. Atmos. 123, 3087–3098. https://doi.org/10.1002/2017JD027661.
Woolway, R.I., Jones, I.D., Hamilton, D.P., Maberly, S.C., Muraoka, K., Read, J.S., Smyth, R.L., Winslow, L.A., 2015. Automated calculation of surface energy fluxes with high-frequency lake buoy data. Environ. Model. Softw. 70, 191–198. https://doi.org/10.1016/j.envsoft.2015.04.013.